ROYAL SOCIETY OF CHEMISTRY

PAPER

Check for updates

First-principles characterization of two-dimensional (CH₃(CH₂)₃NH₃)₂(CH₃NH₃)$_{n-1}$Ge$_n$I$_{3n+1}$ perovskite†

Liyuan Wu,[ab] Pengfei Lu, [ID][a] Yuheng Li,[b] Yan Sun,[b] Joseph Wong[b] and Kesong Yang [ID] *[b]

Two-dimensional (2D) organic–inorganic hybrid perovskites have drawn significant interest due to their great tunability of optoelectronic properties *via* a control of layer dimensionality and high stability compared to their 3D counterparts. Here, we report structural, electronic, excitonic, and optical properties of lead-free 2D Ruddlesden–Popper hybrid perovskites (CH₃(CH₂)₃NH₃)₂(CH₃NH₃)$_{n-1}$Ge$_n$I$_{3n+1}$ (n = 1, 2, and 3) from first-principles calculations. Our results show that the 2D perovskites have a higher stability than their 3D analogous (CH₃NH₃)GeI₃ (n = ∞), and their band gaps decrease with increasing n values, from 1.88 eV (n = 1), to 1.83 eV (n = 2), to 1.69 eV (n = 3), and to 1.57 eV (n = ∞). The 2D perovskites exhibit a strong anisotropic feature, *i.e.*, a low charge carrier effective mass and strong absorption in their 2D planes as compared to that in their third direction. These 2D perovskites also show a high exciton binding energy, allowing for an enhanced photoluminescence quantum efficiency with respect to their 3D compounds. These results suggest a great potential of these germanium-based 2D hybrid perovskites in the optoelectronic applications.

1 Introduction

Conventional three-dimensional (3D) organic–inorganic hybrid perovskites have stimulated considerable interest in the academic and industrial community due to their low fabrication cost and great promising application in optoelectronics.[1–4] The most investigated hybrid perovskite is based on the hybrid lead halide perovskite, such as CH₃NH₃PbI₃, which has reached a power conversion efficiency (PCE) of 21–22% in solar cell devices.[5] However, the long-term prospects of hybrid perovskites still face two major challenges. The first is the water-soluble toxic lead in the champion hybrid lead halide perovskites.[6] The second is the intrinsic instability of hybrid perovskites exposed to moisture, oxygen, heat, and light.[7,8] These challenges drive the development of alternative lead-free halide perovskite materials with improved stability.

In contrast, two-dimensional (2D) Ruddlesden–Popper organic–inorganic hybrid perovskites have recently emerged as promising alternatives due to their excellent environmental stability. The origin of the Ruddlesden–Popper structure can be

traced back to the 1950s when Ruddlesden and Popper discovered three compounds with the K₂NiF₄-type structure, such as Sr₂TiO₄, Ca₂MnO₄, and SrLaAlO₄.[9,10] The general formula of 2D hybrid perovskites is (RNH₃)₂A$_{n-1}$M$_n$X$_{3n+1}$ (n = 1, 2, 3,…), where RNH₃ is a large aliphatic or aromatic alkylammonium spacer cation, such as, phenylethylammonium (PEA) and butylammonium (CH₃(CH₂)₃NH₃, *i.e.*, BA), A is a monovalent organic cation, typically CH₃NH₃ (MA), M is a divalent metal cation, X is a halide anion, and n represents the number of MX₆⁴⁻ octahedral layers between two layers of the organic chains. The hydrophobicity of the long organic chains greatly enhances the moisture resistance of 2D perovskites relative to their 3D analogue.[11] Moreover, 2D perovskites can be regarded as quantum-wells in which the semiconducting inorganic layers act as potential wells and the insulating organic layers as potential barriers.[12]

The unique crystal structure of 2D perovskites leads to many tunable optoelectronic properties, inducing strong exciton binding energies and high quantum efficiencies, which have been used in optoelectronic devices such as field-effect transistors (FETs),[13,14] light-emitting diodes (LEDs),[15] and photodetectors.[16] In the realm of photovoltaics, 2D perovskites show poor PCE at 2.5–4.73% because of inhibited out-of-plane charge transport caused by insulating organic spacing layers such as PEA and BA.[17–19] One possible approach to overcome this issue is to fabricate high-quality thin films with preferential cross-plane alignment. For example, Tsai *et. al.* fabricated a solar

[a]State Key Laboratory of Information Photonics and Optical Communications, Beijing University of Posts and Telecommunications, Beijing 100876, China

[b]Department of NanoEngineering, University of California San Diego, 9500 Gilman Drive, Mail Code 0448, La Jolla, California 92093-0448, USA. E-mail: kesong@ucsd.edu

† Electronic supplementary information (ESI) available. See DOI: 10.1039/c8ta10055a

This journal is © The Royal Society of Chemistry 2018

J. Mater. Chem. A, 2018, 6, 24389–24396 | 24389

cell device based on the 2D layered perovskite $(BA)_2(MA)_{n-1}$-Pb_nI_{3n+1} ($n = 4$) with a high PCE of 12.52% using this strategy.[20]

There have been trial experimental efforts to prepare environment-friendly lead-free compounds by substituting the divalent Pb with Sn.[19,21,22] Some preliminary first-principles-based computational studies have also been carried out to explore the materials properties of tin- and germanium-based 2D hybrid perovskites.[23–25] As a similar compound to group IVA Pb and Sn-based perovskites, Ge-based perovskites may exhibit analogous properties as Pb- and Sn-based counterparts. The ionic radius of Ge is much smaller than that of Sn and Pb, leading to a greater diversity in structure and performance.[26,27] However, Ge has rarely been used to develop two-dimensional perovskites. In 1996, Mitzi investigated the crystal structure and optical properties of a layered Ge-based perovskite, $(BA)_2GeI_4$. Its photoluminescence spectrum was found to peak around 690 nm (1.80 eV), but its photoelectric behavior remains unclear.[28] Recently, Kanatzidis *et al.* synthesized a series of Ge-based perovskites with 3D frameworks and 1D infinite chains, in which, unfortunately, 2D homologous structures were not formed due to the lack of long organic molecules.[29] Very recently, with the incorporation of PEA, Cheng *et al.* synthesized 2D $(PEA)_2GeI_4$ and investigated its structure and photoelectric properties, identifying the potential of 2D germanium halide perovskites for photovoltaic applications.[30]

In this work, we employed first-principles calculations to investigate the structural, electronic, excitonic, and optical properties of the sparsely explored series of 2D Ruddlesden–Popper lead-free perovskites $(BA)_2(MA)_{n-1}Ge_nI_{3n+1}$ ($n = 1, 2, 3$). We carry out the work in the following steps. First, we investigated the geometrical structures and calculated the decomposition energies compared to the 3D counterpart. Then, we studied the band gaps, carrier effective masses and exciton binding energies of the $(BA)_2(MA)_{n-1}Ge_nI_{3n+1}$ series. Lastly, we investigated their optical absorption along the in-plane and out-of-plane directions.

2   Computational details

Our first-principles calculations were performed using the Vienna Ab initio Simulation Package (VASP).[31] The projected augmented wave (PAW) potentials were used to analyze the interactions between core electrons and valence electrons.[32] We tested structure relaxation using two functional: the Perdew–Burke–Ernzerhof (PBE) within the generalized gradient approximation (GGA),[33] and PBE with dispersion interactions included *via* Grimme's D3 dispersion correction (PBE + D3).[34] The plane-wave energy cutoff was set to be 450 eV. The convergence criterion for a total energy was set as 10^{-5} eV. All the atomic positions and lattice structures were fully relaxed with the threshold of a maximum force of 0.02 eV Å^{-1}. A Gamma-centered k-point mesh with a Monkhorst–Pack scheme from $6 \times 6 \times 1$ to $4 \times 4 \times 1$ was employed.[35] Heyd–Scuseria–Ernzerhof hybrid functional (HSE06)[36,37] was employed to obtain a more accurate description of the electronic structure and optical properties. The high-frequency dielectric constants were computed using density-functional perturbation theory

(DFPT)[38] based upon a tightly converged electronic wave-function (within 10^{-7} eV) and a denser grid of k-point mesh.

3   Results and discussion

3.1   Geometric structures

2D perovskites can conceptually be derived from specific cuts or slices of the 3D perovskite structures.[39] A 2D hybrid perovskite can be regarded as n layers of MX_6^{4-} octahedral sheets sandwiched by two layers of large organic spacer cations. In principle, the inorganic MX_6^{4-} octahedral layers can be obtained by slicing the cubic AMX_3 structure along the (001) plane and the large organic spacer cations can be introduced by replacing the MA cations at the edges. In this work, by employing the structure prototypes of Ruddlesden–Popper perovskites, we built the 2D $(BA)_2(MA)_{n-1}Ge_nI_{3n+1}$ models by stacking two single 2D perovskite layers with a misshift of a half of lattice constant along the in-plane direction. Its in-plane unit cell adopts a $\sqrt{2} \times \sqrt{2}$ supercell of the cubic $MAGeI_3$, that is, $a = b = \sqrt{2}a_0$, in which a_0 is the lattice constant of cubic $MAGeI_3$. n refers to the number of inorganic layers, which determines the lattice constant c of the 2D perovskite. The structural models at $n = 1$, 2, and 3 are shown in Fig. 1(a–c). At $n = \infty$, the 2D perovskite model is equivalent to its parental 3D compound, $MAGeI_3$, see Fig. 1(d). Note that to have an intuitive understanding of tendency from 2D to 3D perovskites, a $\sqrt{2} \times \sqrt{2} \times 3$ supercell was shown here and also employed for the electronic structure calculations, as discussed later.

In the 2D perovskite $(BA)_2(MA)_{n-1}Ge_nI_{3n+1}$, there are two types of organic molecules, the short MA and long BA. According to the ordering and configurations of ammonium heads of BA cations, that is, the relative positions between the hydrogen bond and halide octahedral, we built two types of structural models for the 2D perovskites, see Fig. S1 in the ESI.† In the model I, all the ammonium heads are along the same direction; in the model II, the ammonium heads have an alternative order, which agrees with the found structure in the experiment.[28] The geometry structures of the two models were firstly relaxed using standard DFT calculations with the PBE functional. It is found that model II is energetically more favorable than model I by ~2 meV per atom, and the lattice parameter c of model II is much closer to the experimental value than that of model I,[28] as shown in Tables S1 and S2 in the ESI.† Therefore, the model II was selected for further investigation in this work.

In addition, considering the van der Waals (vdW) interaction of the organic cations between the perovskite layers,[40] we also relaxed structures using Grimme's D3 dispersion correction on the PBE functional (PBE + D3).[34] This approach has been proved to be capable of predicting reasonable lattice constants of 2D perovskites.[24,41] The calculated lattice parameters of the 2D perovskites $(BA)_2(MA)_{n-1}Ge_nI_{3n+1}$ ($n = 1$, 2, and 3) are shown in Table 1. At $n = 1$, the lattice constant c of $(BA)_2GeI_4$ is calculated to be 29.109 Å with PBE functional, and was further improved as 28.438 Å with D3 correction, and the latter is much more consistent with the experimental value of 28.014 Å.[28] As n increases, the lattice constants a and b both increase, from
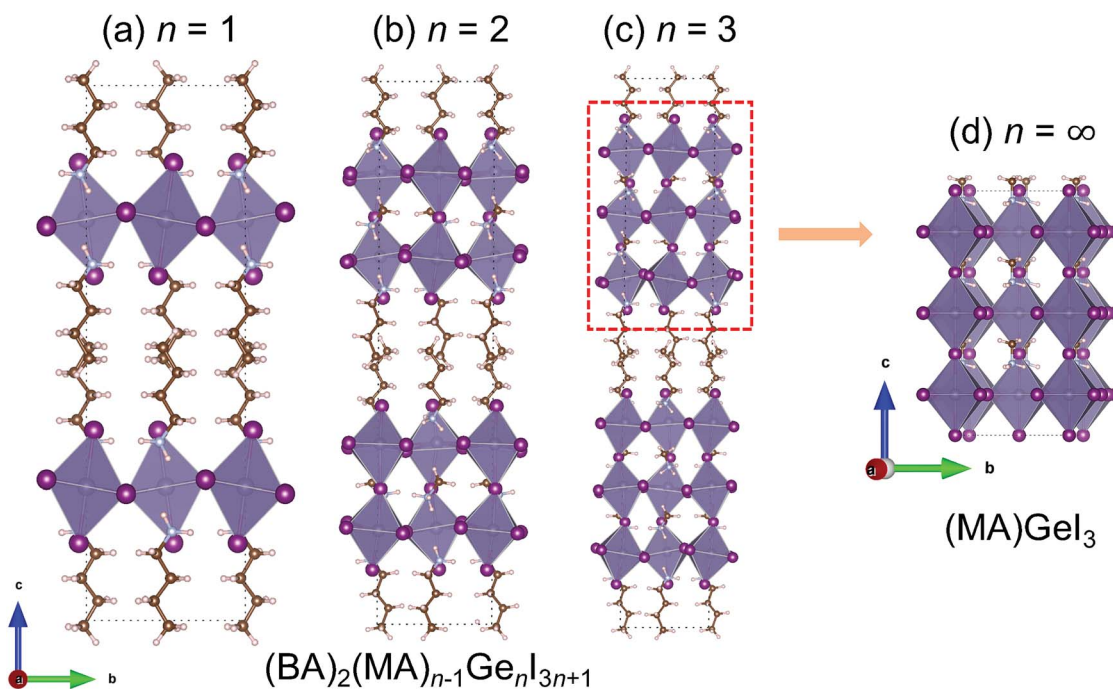
Fig. 1 Crystal structures of relaxed two-dimensional (2D) hybrid germanium perovskite $(BA)_2(MA)_{n-1}Ge_nI_{3n+1}$ with (a) $n = 1$, (b) $n = 2$, and (c) $n = 3$. At (d) $n = \infty$, the 2D structures become 3D compound $(MA)GeI_3$. To have an intuitive view of the structural evolution, a $\sqrt{2} \times \sqrt{2} \times 3$ supercell of the cubic primitive $MAGeI_3$ is used to show the 3D model.

7.957 Å ($n = 1$) to 8.478 Å ($n = \infty$) and from 8.45 Å ($n = 1$) to 8.580 Å ($n = \infty$), respectively, while the distance between two perovskite layers decreases, from 8.243 Å ($n = 1$) to 8.039 Å ($n = 2$) and 8.036 Å ($n = 3$). At $n = 1$, the incorporation of BA molecules makes the octahedra GeI_6^{4-} alternately tilt along the b axis after relaxation, which makes the bulk $(BA)_2GeI_4$ have an orthorhombic lattice with $\alpha = \beta = \gamma = 90°$. At $n \geq 2$, the incorporation of MA molecules into the inorganic GeI_6^{4-} framework leads to a distortion of the lattice, with the lattice parameters α, β, and γ away from 90°. At $n = \infty$, the 2D hybrid

perovskite can be considered as 3D $MAGeI_3$ structure, which has the strongest lattice distortion, as shown in Table 1.

Next, we examined the stability of the 2D hybrid perovskites by calculating their decomposition energy with respect to the decomposed components (GeI_2, MAI and BAI) using the following equations:

$$E_{d,2D} = \frac{2E_{BAI} + nE_{GeI_2} + (n-1)E_{MAI} - E_{total}}{n} \quad (1)$$

where $E_{d,2D}$ refers to the decomposition energy, E_{GeI_2}, E_{MAI}, and E_{BAI} are the total energies of their bulk GeI_2, MAI and BAI, respectively, E_{total} is the total energy of the 2D hybrid perovskite, and n is the number of inorganic layers. At $n = \infty$, the decomposition energy can be rewritten as:

$$E_{d,3D} = E_{GeI_2} + E_{MAI} - E_{total} \quad (2)$$

The calculated decomposition energies are 1.13, 0.69, 0.62, and 0.23 eV for $n = 1$, $n = 2$, $n = 3$, and $n = \infty$, respectively, as summarized in Table 2. These results indicate that the 2D hybrid perovskites are stable against the components. Compared with 3D perovskite ($n = \infty$), 2D perovskites show much higher decomposition energies and much higher stability, consistent with the finding in other 2D perovskites.[42] To explore the origin of the high stability in the 2D perovskites, we carried out a Bader charge analysis[43] for the 2D $(BA)_2GeI_4$ and 3D $MAGeI_3$, as shown in Fig. S2 of ESI.† For $(BA)_2GeI_4$, the calculated Bader charge is −0.57 for I anion in the BAI layer and +0.69 for Ge cation in the GeI_2 layer. For $MAGeI_3$, the calculated Bader charge is −0.46 for I anion in the MAI layer and +0.67 for

Table 1 Lattice parameters of 2D $(BA)_2(MA)_{n-1}Ge_nI_{3n+1}$ and 3D $MAGeI_3$ perovskites, calculated using PBE functional and PBE functional with Grimme's D3 dispersion correction (PBE + D3). Exp. represents the experimental value

Compounds	Functional	a (Å)	b (Å)	c (Å)	α (°)	β (°)	γ (°)
$(BA)_2GeI_4$	PBE	8.164	8.547	29.109	90.0	90.0	90.0
	PBE + D3	7.957	8.450	28.438	90.0	90.0	90.0
	Exp.[28]	8.272	8.722	28.014	90.0	90.0	90.0
$(BA)_2(MA)Ge_2I_7$	PBE	8.454	8.777	41.183	89.6	90.7	89.6
	PBE + D3	8.211	8.526	40.243	89.7	90.8	89.8
$(BA)_2(MA)_2Ge_3I_{10}$	PBE	8.393	8.714	54.192	89.0	89.8	90.2
	PBE + D3	8.239	8.514	52.775	89.2	89.6	90.1
$MAGeI_3{}^a$	PBE	8.735	8.856	19.062	86.2	88.4	88.7
	PBE + D3	8.478	8.580	18.367	86.3	87.6	89.4
	Exp.[29]	8.553	8.553	11.162	90.0	90.0	120.0

^{a} To have an intuitive comparison between the 2D and 3D perovskites, a $\sqrt{2} \times \sqrt{2} \times 3$ supercell of cubic $MAGeI_3$ was employed in our calculations. The 3D $MAGeI_3$ structure in ref. 29 adopts a $\sqrt{2} \times \sqrt{2} \times \sqrt{3}$ supercell.

This journal is © The Royal Society of Chemistry 2018

J. Mater. Chem. A, 2018, **6**, 24389–24396 | **24391**

Table 2 Decomposition energies (E_d), band gaps (E_g), electron (m_e) and hole (m_h) effective masses, high-frequency dielectric constants (ε) and exciton binding energies (E_b) of 2D $(BA)_2(MA)_{n-1}Ge_nI_{3n+1}$ and 3D $MAGeI_3$ perovskites

Compounds	E_d (eV)	E_g (eV)	m_e (m_0) Γ–X/Γ–Y	m_h (m_0) Γ–X/Γ–Y	ε	E_b (meV)
$(BA)_2GeI_4$	1.13	1.88	0.19/0.18	0.28/0.27	5.46	202
$(BA)_2(MA)Ge_2I_7$	0.69	1.83	0.23/0.14	0.34/0.31	5.81	190
$(BA)_2(MA)_2Ge_3I_{10}$	0.62	1.69	0.22/0.13	0.27/0.26	6.15	150
$MAGeI_3$	0.23	1.57	0.22/0.20	0.28/0.31	7.02	34

Ge cation in the GeI_2 layer. These results indicate that there is more charge transfer from Ge cations to I anions in the 2D $(BA)_2GeI_4$ than that in the 3D $MAGeI_3$, indicating a stronger bonding strength between GeI_2 and BAI layers than that between GeI_2 and MAI layers and thus a higher stability in the 2D $(BA)_2GeI_4$. This can be fundamentally attributed to the different electropositivity between BA and MA organic cations. Compared to MA, the BA has a weaker electropositivity and thus donates fewer electrons to the I anions in the BAI layer, which determines that the I anions in the BA layer can capture more electrons from the adjacent Ge cations in the GeI_2 layers. As n increases, namely incorporating more MAI layers in the $(BA)_2(MA)_{n-1}Ge_nI_{3n+1}$, the relative number of BA layers decreases, and thus the stability of 2D perovskite decrease, which is consistent with the trend for the calculated decomposition energy.

3.2 Electronic properties

Next, we investigated the electronic structures of 2D $(BA)_2(MA)_{n-1}Ge_nI_{3n+1}$ and 3D $MAGeI_3$ perovskites, calculated using the HSE06 functional. As with other 2D perovskites,[19,44] the band gaps of $(BA)_2(MA)_{n-1}Ge_nI_{3n+1}$ decrease monotonically as the thickness of the inorganic layer increases, from 1.88 eV

($n = 1$), to 1.83 eV ($n = 2$), 1.69 eV ($n = 3$), and 1.57 eV ($n = \infty$), as listed in Table 2. It clearly shows that 2D compounds have a larger band gap than the 3D perovskite. The calculated band gap of $(BA)_2GeI_4$ is consistent with the photoluminescence spectral peak value at 690 nm (1.80 eV) in experiment.[28] The tunable band gaps as a function of n can be understood from the quantum confinement effects.[44] The 2D hybrid perovskites behave like quantum wells, with inorganic layers as potential wells and insulating organic layers as potential barriers.[12] As n reduces from ∞ to 1, the thickness of inorganic layers reduces, and thus the band gap increases. The corresponding band structures are shown in Fig. 2, the relative contribution of Ge and I are marked by color, where green (red) corresponds to the state originating from Ge(I). It can be observed visually that the conduction band derives from the contribution of Ge, while the valence band results almost entirely from I contribution and a small amount from Ge contribution. All the compounds have direct band gaps with both the conduction band minimum (CBM) and valence band maximum (VBM) located at Γ points for 2D perovskites and at Z (0,0,0.5) point for the 3D perovskite.

To gain a better understanding of the origin of the conduction band and valence band, we plotted the density of states (DOS) and partial DOS of 2D perovskite $(BA)_2GeI_4$ as shown in Fig. 3. The contribution of BA molecules to the DOS is mainly
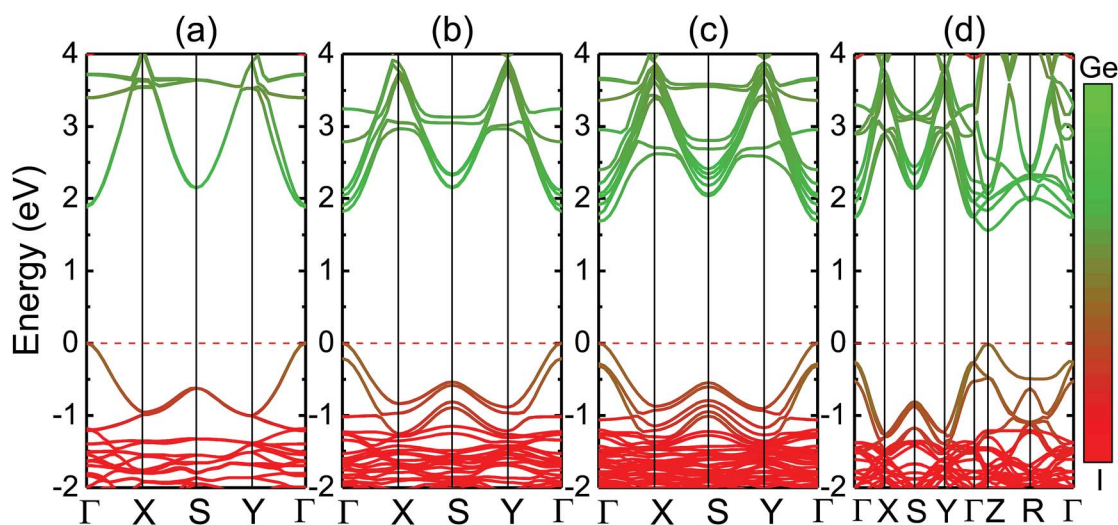

Fig. 2 Calculated HSE06 projected-band structures of 2D $(BA)_2(MA)_{n-1}Ge_nI_{3n+1}$ and 3D $MAGeI_3$ perovskites, (a) $(BA)_2GeI_4$, (b) $(BA)_2(MA)Ge_2I_7$, (c) $(BA)_2(MA)_2Ge_3I_{10}$ and (d) $MAGeI_3$, along the $\Gamma(0,0,0)$–$X(0.5,0,0)$–$S(0.5,0.5,0)$–$Y(0,0.5,0)$–$\Gamma(0,0,0)$–$Z(0,0,0.5)$–$R(0.5,0.5,0.5)$ path through the first Brillouin zone. The Fermi level is set to be 0 eV and indicated by the red horizontal dash line. The relative contribution of Ge and I are marked by color, in which green (red) corresponds to the state originating from Ge(I). Note that a $\sqrt{2} \times \sqrt{2} \times 3$ supercell of the cubic primitive $MAGeI_3$ is used to calculate the electronic band structure for a clear comparison with the 2D perovskites.
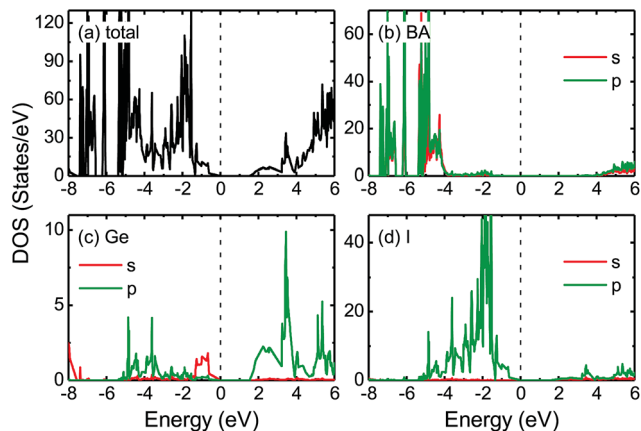
24392 | *J. Mater. Chem. A*, 2018, **6**, 24389–24396

This journal is © The Royal Society of Chemistry 2018

Fig. 3 Density of states (DOS) of $(BA)_2GeI_4$. (a) Total DOS, and partial DOS of (b) molecule, (c) Ge, and (d) I. Red and green lines donate the s and p contribution, respectively. The Fermi level is indicated by the black vertical dash line.

Fig. 4 Top views of decomposed charge densities of (a) CBM and (b) VBM of $(BA)_2GeI_4$, and the corresponding side views (a') and (b'). The isosurface level is 0.0015 e per $Bohr^3$. The C, H and N atoms are not shown for the clear display.

located at low energy region of valence band from -8 to -4 eV, far away from the band edges, as shown in Fig. 3(b), indicating that organic molecules do not have a direct influence on the band gaps of 2D perovskites, which is consistent with other type of organic–inorganic perovskite.[45] Fig. 3(c and d) illustrate that the conduction band is mostly composed of Ge 4p states, while the valence band is mainly composed of I 5p states and a small amount of Ge 4s, which is in an agreement with the band contribution in Fig. 2. This can also be observed through the decomposed charge densities of CBM and VBM in Fig. 4. Therefore, our results show that the band gaps of 2D $(BA)_2(MA)_{n-1}Ge_nI_{3n+1}$ perovskites are primarily determined by distorted inorganic MX_6^{4-} octahedral and that the organic molecules do not take part in the formation of the valence band nor the conduction band. However, the inorganic MX_6^{4-} framework can be affected by the organic molecule design, such as alkyl chain length, insertion of π-conjugated segment, and ammonium dications, which in turn greatly impact the optoelectronic properties.[46] The DOS and decomposed charge densities of $(BA)_2(MA)Ge_2I_7$ and $(BA)_2(MA)_2Ge_3I_{10}$ can be found in Fig. S3–S6 of the ESI.†

We next estimated the hole and electron effective mass (m) by using the following equation,

$$m = \frac{\hbar^2 \partial k^2}{\partial^2 E(k)} \tag{3}$$

where $\hbar$ is the reduced Planck constant, $E(k)$ are the eigenvalues at band edges around the VBM and CBM, and k is the wave vector. The calculated hole (m_h) and electron (m_e) effective masses are listed in Table 2. Since the bands near the valence and conduction edges are dispersive along the directions parallel to the perovskite layers (Γ–X and Γ–Y), both m_e and m_h have small values along x and y directions. On the other hand, in the perpendicular direction (Γ–Z), the inorganic semiconducting network is disconnected and has nearly flat bands along this direction, meaning the effective masses along this direction are extremely large. This indicates that charge
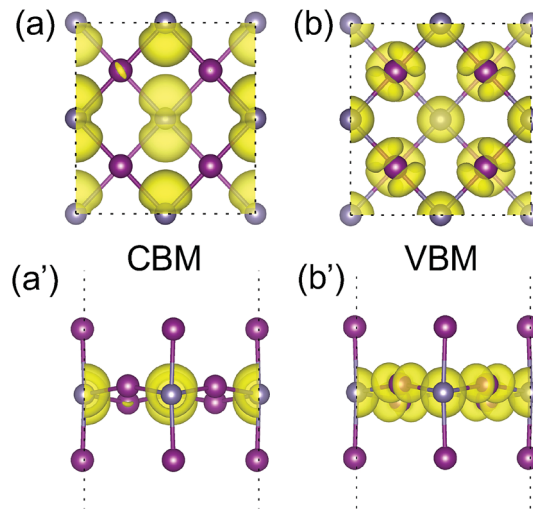
transport tends to be restricted to the ab-plane. The calculated masses of 2D $(BA)_2(MA)_{n-1}Ge_nI_{3n+1}$ perovskites do not have a clear trend and are independent of the layer number n, which is consistent with the previous results of $(BA)_2(MA)_{n-1}Pb_nI_{3n+1}$.[44] However, the average electron effective masses for 2D perovskites is smaller than the 3D perovskite.

Next, we estimated the exciton binding energy using the semiclassical Wannier–Mott theory.[47,48] Note that the excitons can extend freely in the 3D bulk materials but are tightly confined in the planes of 2D materials or thin films.[49,50] This is because of the significant difference between the in-plane and out-of-plane high-frequency dielectric constants for the 2D materials, which further leads to a complex Wannier–Mott problem that has been discussed previously in detail.[51,52] The exciton binding energy of the 2D material (considering quantum confinement) can then be estimated by a factor of four relative to the analogous 3D perovskites.[53,54] Considering the 3D perovskite with the same high-frequency dielectric constant and reduced effective mass as the 2D perovskite, we estimated the exciton binding energies (E_b) by using the following equations,

$$E_{b,2D} = 4 \times E_{b,3D} = 4 \times \frac{\mu e^4}{2\hbar^2 \varepsilon^2} \tag{4}$$

where ε is the planar high-frequency dielectric constant, $\mu = m_e \times m_h/(m_e + m_h)$ is the reduced effective mass and e is the charge of electron. Here, m_e and m_h are adopted as the average value in the xy plane.

The calculated ε and E_b are summarized in Table 2. We can see that ε increases with increasing layers of 2D sheets, from 5.46($n = 1$), to 5.81($n = 2$), 6.15($n = 3$) and 7.02($n = \infty$). This is attributed to the dielectric confinement resulting from low dielectric constant of the organic part and high dielectric constant of the inorganic part. The exciton binding energies are 202, 190, 150, and 34 meV for $n = 1$, $n = 2$, $n = 3$, and $n = \infty$, respectively. The value of 202 meV when $n = 1$ is consistent with

the reported 231 meV value of single-layer BA_2GeI_4.[41] The exciton binding energy is larger than that of 3D perovskite, owing to the quantum and dielectric confinement. The large exciton binding energies (150–202 meV) indicate that the exciton effect in the 2D perovskites ($n \leq 3$) is strong. Such a strong exciton effect may enable the enhanced PL quantum efficiency at room temperature, implying they are suitable for LED devices.[55] Note that despite the high exciton binding energies, such strong excitonic 2D perovskites may also be useful as photovoltaic solar cells materials if they are in contact with appropriate transport layers.[56] Note that at high n values, the compound becomes a quasi 2D or 3D structure, the exciton binding energy can no longer be estimated by multiplying a factor of four. Instead, the exciton binding energies will be close to that of $MAGeI_3$ ($n = \infty$), which is consistent with the prediction in 2D lead-based perovskites.[20]

3.3 Optical properties

In this section, we investigated the optical properties of 2D $(BA)_2(MA)_{n-1}Ge_nI_{3n+1}$ perovskites. The optical properties can be obtained from dielectric functions, which are usually used to describe the linear response of the crystal system to electromagnetic radiation. The imaginary part $\varepsilon_2(\omega)$ of the dielectric function is derived from the appropriate momentum matrix elements between the occupied and the unoccupied wave functions within the selection rules over the Brillouin zone, and the real part $\varepsilon_1(\omega)$ of dielectric function follows the Kramer–Kronig relationship. Thus, the absorption coefficient $\alpha(\omega)$ is determined by the following equation,[57]

$$\alpha(\omega) = \sqrt{2}\,\frac{\omega}{c}\sqrt{\sqrt{\varepsilon_1(\omega)^2 + \varepsilon_2(\omega)^2} - \varepsilon_1(\omega)} \qquad (5)$$

where ω is the photon frequency, and c is the speed of light in the vacuum.

Based on the electronic ground state calculations at HSE06 level, we obtained $\varepsilon_2(\omega)$ and $\varepsilon_1(\omega)$ of dielectric function. The calculated energy dependence of the optical absorption coefficient is shown in Fig. 5. The comparison absorption spectra of 2D perovskites for the light polarized parallel to xy plane is shown in Fig. 5(a). As expected from the behavior of the calculated band gap, we found a redshift of the absorption edges with increasing n values, from 1.96 eV ($n = 1$), to 1.81 eV ($n = 2$), and 1.79 eV ($n = 3$). The absorption coefficient reaches 10^5 cm^{-1} quickly near the band edge, especially for $n = 2$ and 3, indicating their strong optical absorption in the visible light region (1.77–3.18 eV) in the xy plane. For $n = 1$, see Fig. 5(b), the optical absorption in the x and y directions coincide exactly, likely originating from the perfect centrosymmetric structure after structural relaxation. For $n = 2$ and 3, see Fig. 5(c and d), the optical absorption exhibits a nuance between the x and y directions, which is caused by the noncentrosymmetric structure due to the existence of disordered MA molecules among the GeI_6^{4-} octahedrons.

For all the 2D counterparts, the optical absorption showed an obvious difference between the in-plane (x and y) and out-of-plane (z) directions, as seen in Fig. 5(b–d). In the x and y
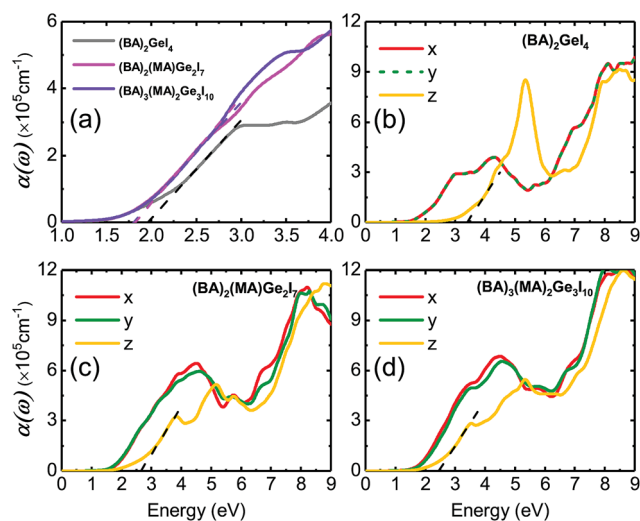

Fig. 5 Calculated optical absorption spectra $\alpha(\omega)$ of 2D perovskites: (a) comparison $\alpha(\omega)$ of all the 2D perovskites for the light polarized parallel to xy plane; (b–d) $\alpha(\omega)$ of $(BA)_2GeI_4$, $(BA)_2(MA)Ge_2I_7$, $(BA)_2(MA)_2Ge_3I_{10}$ for the incident light polarized along x, y and z directions, respectively. The dashed lines show an approximate linear fit to estimate the band edges for the first absorption peak.

directions, 2D perovskites exhibit strong optical absorption, which increases in strength with increasing n. In the z direction, however, they have weak optical absorption in the visible light region. Especially for $(BA)_2GeI_4$, the onset of absorption in z direction is about 3.41 eV, which is out of the visible region, indicating poor light absorption in this direction, see Fig. 5(b). When n increases, the onset of absorption in z direction has a redshift, from 3.41 eV ($n = 1$), to 2.65 eV ($n = 2$), and to 2.45 eV ($n = 3$), as shown in Fig. 5(b–d), indicating enhanced visible light absorption along z direction with the increasing inorganic layers ($n \geq 2$). As a result, with n reaching ∞, it is expected that there will be no difference in the optical absorption between the in-plane and out-of-plane directions. The anisotropy of the optical absorption can also be explained from the significant difference of the dielectric constant between the organic BA molecules and inorganic layers, as discussed in the section of exciton binding energy. In short, the 2D perovskites exhibit a strong in-plane optical absorption and weak optical absorption along the out-of-plane direction. As the number of inorganic layers n increases, there is a considerable optical absorption in the visible region, indicating potential applications for photovoltaic solar cells with appropriate crystal orientations.

4 Conclusion

In summary, we have investigated the structural, electronic, excitonic and optical properties of lead-free 2D Ruddlesden–Popper perovskites $(BA)_2(MA)_{n-1}Ge_nI_{3n+1}$ using first-principles electronic structure calculations. Our results show that 2D perovskites have a larger decomposition energy than their 3D counterparts, showing an enhanced stability. The 2D perovskites have direct band gaps in the range from 1.88 eV ($n = 1$), to

1.83 eV ($n = 2$) and to 1.69 eV ($n = 3$), with an exciton binding energy of 150~202 meV ($n \leq 3$) that is much larger than that of 3D counterpart (34 meV). These 2D perovskites also exhibit a small charge carrier effective mass and a strong optical absorption in their 2D planes compared to that in their third dimension, showing a strong anisotropy feature and promising applications in the optoelectronic devices.

Conflicts of interest

There are no conflicts to declare.

Acknowledgements

References

1 M. A. Green, A. Ho-Baillie and H. J. Snaith, *Nat. Photonics*, 2014, **8**, 506–514.

2 N.-G. Park, *Mater. Today*, 2015, **18**, 65–72.

3 Z. Xiao, Y. Yuan, Y. Shao, Q. Wang, Q. Dong, C. Bi, P. Sharma, A. Gruverman and J. Huang, *Nat. Mater.*, 2015, **14**, 193–198.

4 Y. Fang, Q. Dong, Y. Shao, Y. Yuan and J. Huang, *Nat. Photonics*, 2015, **9**, 679–686.

5 D. Bi, C. Yi, J. Luo, J.-D. Décoppet, F. Zhang, S. M. Zakeeruddin, X. Li, A. Hagfeldt and M. Grätzel, *Nat. Energy*, 2016, **1**, 16142.

6 A. Babayigit, A. Ethirajan, M. Muller and B. Conings, *Nat. Mater.*, 2016, **15**, 247.

7 H.-S. Kim, J.-Y. Seo and N.-G. Park, *ChemSusChem*, 2016, **9**, 2528–2540.

8 T. Leijtens, G. E. Eperon, N. K. Noel, S. N. Habisreutinger, A. Petrozza and H. J. Snaith, *Adv. Energy Mater.*, 2015, **5**, 1500963.

9 S. Ruddlesden and P. Popper, *Acta Crystallogr.*, 1957, **10**, 538–539.

10 S. Ruddlesden and P. Popper, *Acta Crystallogr.*, 1958, **11**, 54–55.

11 D. Bi, P. Gao, R. Scopelliti, E. Oveisi, J. Luo, M. Grätzel, A. Hagfeldt and M. K. Nazeeruddin, *Adv. Mater.*, 2016, **28**, 2910–2915.

12 X. Hong, T. Ishihara and A. Nurmikko, *Phys. Rev. B: Condens. Matter Mater. Phys.*, 1992, **45**, 6961.

13 C. R. Kagan, D. B. Mitzi and C. D. Dimitrakopoulos, *Science*, 1999, **286**, 945–947.

14 C. Chen, X. Zhang, G. Wu, H. Li and H. Chen, *Adv. Opt. Mater.*, 2017, **5**, 1600539.

15 M. Yuan, L. N. Quan, R. Comin, G. Walters, R. Sabatini, O. Voznyy, S. Hoogland, Y. Zhao, E. M. Beauregard, P. Kanjanaboos, *et al.*, *Nat. Nanotechnol.*, 2016, **11**, 872.

16 Z. Tan, Y. Wu, H. Hong, J. Yin, J. Zhang, L. Lin, M. Wang, X. Sun, L. Sun, Y. Huang, *et al.*, *J. Am. Chem. Soc.*, 2016, **138**, 16612–16615.

17 I. C. Smith, E. T. Hoke, D. Solis-Ibarra, M. D. McGehee and H. I. Karunadasa, *Angew. Chem., Int. Ed.*, 2014, **53**, 11232–11235.

18 D. H. Cao, C. C. Stoumpos, O. K. Farha, J. T. Hupp and M. G. Kanatzidis, *J. Am. Chem. Soc.*, 2015, **137**, 7843–7850.

19 D. H. Cao, C. C. Stoumpos, T. Yokoyama, J. L. Logsdon, T.-B. Song, O. K. Farha, M. R. Wasielewski, J. T. Hupp and M. G. Kanatzidis, *ACS Energy Lett.*, 2017, **2**, 982–990.

20 H. Tsai, W. Nie, J.-C. Blancon, C. C. Stoumpos, R. Asadpour, B. Harutyunyan, A. J. Neukirch, R. Verduzco, J. J. Crochet, S. Tretiak, *et al.*, *Nature*, 2016, **536**, 312.

21 K. P. Marshall, R. I. Walton and R. A. Hatton, *J. Mater. Chem. A*, 2015, **3**, 11631–11640.

22 T. Yokoyama, D. H. Cao, C. C. Stoumpos, T.-B. Song, Y. Sato, S. Aramaki and M. G. Kanatzidis, *J. Phys. Chem. Lett.*, 2016, **7**, 776–782.

23 Z.-Q. Ma, Y. Shao, P. K. Wong, X. Shi and H. Pan, *J. Phys. Chem. C*, 2018, **122**, 5844–5853.

24 Z. Wang, A. M. Ganose, C. Niu and D. O. Scanlon, *J. Mater. Chem. A*, 2018, **6**, 5652–5660.

25 L. Ma, M.-G. Ju, J. Dai and X. C. Zeng, *Nanoscale*, 2018, **10**, 11314–11319.

26 D. Trots and S. Myagkota, *J. Phys. Chem. Solids*, 2008, **69**, 2520–2526.

27 I. Chung, J.-H. Song, J. Im, J. Androulakis, C. D. Malliakas, H. Li, A. J. Freeman, J. T. Kenney and M. G. Kanatzidis, *J. Am. Chem. Soc.*, 2012, **134**, 8579–8587.

28 D. B. Mitzi, *Chem. Mater.*, 1996, **8**, 791–800.

29 C. C. Stoumpos, L. Frazer, D. J. Clark, Y. S. Kim, S. H. Rhim, A. J. Freeman, J. B. Ketterson, J. I. Jang and M. G. Kanatzidis, *J. Am. Chem. Soc.*, 2015, **137**, 6804–6819.

30 P. Cheng, T. Wu, J. Zhang, Y. Li, J. Liu, L. Jiang, X. Mao, R.-F. Lu, W.-Q. Deng and K. Han, *J. Phys. Chem. Lett.*, 2017, **8**, 4402–4406.

31 G. Kresse and J. Furthmüller, *Phys. Rev. B: Condens. Matter Mater. Phys.*, 1996, **54**, 11169–11186.

32 G. Kresse and D. Joubert, *Phys. Rev. B: Condens. Matter Mater. Phys.*, 1999, **59**, 1758–1775.

33 J. P. Perdew, K. Burke and M. Ernzerhof, *Phys. Rev. Lett.*, 1996, **77**, 3865–3868.

34 S. Grimme, J. Antony, S. Ehrlich and H. Krieg, *J. Chem. Phys.*, 2010, **132**, 154104.

35 H. J. Monkhorst and J. D. Pack, *Phys. Rev. B: Condens. Matter Mater. Phys.*, 1976, **13**, 5188–5192.

36 J. Heyd, G. E. Scuseria and M. Ernzerhof, *J. Chem. Phys.*, 2003, **118**, 8207–8215.

This journal is © The Royal Society of Chemistry 2018

J. Mater. Chem. A, 2018, **6**, 24389–24396 | 24395

37 A. V. Krukau, O. A. Vydrov, A. F. Izmaylov and G. E. Scuseria, *J. Chem. Phys.*, 2006, **125**, 224106.

38 S. Baroni, S. de Gironcoli, A. Dal Corso and P. Giannozzi, *Rev. Mod. Phys.*, 2001, **73**, 515–562.

39 D. B. Mitzi, *J. Chem. Soc., Dalton Trans.*, 2001, 1–12.

40 D. B. Mitzi, K. Chondroudis and C. R. Kagan, *IBM J. Res. Dev.*, 2001, **45**, 29–45.

41 L. Ma, J. Dai and X. C. Zeng, *Adv. Energy Mater.*, 2017, **7**, 1601731.

42 L. N. Quan, M. Yuan, R. Comin, O. Voznyy, E. M. Beauregard, S. Hoogland, A. Buin, A. R. Kirmani, K. Zhao, A. Amassian, D. H. Kim and E. H. Sargent, *J. Am. Chem. Soc.*, 2016, **138**, 2649–2655.

43 W. Tang, E. Sanville and G. Henkelman, *J. Phys.: Condens. Matter*, 2009, **21**, 084204.

44 C. C. Stoumpos, D. H. Cao, D. J. Clark, J. Young, J. M. Rondinelli, J. I. Jang, J. T. Hupp and M. G. Kanatzidis, *Chem. Mater.*, 2016, **28**, 2852–2867.

45 C. Bernal and K. Yang, *J. Phys. Chem. C*, 2014, **118**, 24383–24388.

46 Y. Chen, Y. Sun, J. Peng, J. Tang, K. Zheng and Z. Liang, *Adv. Mater.*, 2018, **30**, 1703487.

47 G. H. Wannier, *Phys. Rev.*, 1937, **52**, 191–197.

48 N. Mott, *Proc. R. Soc. London, Ser. A*, 1938, **167**, 384–391.

49 M. Shishkin and G. Kresse, *Phys. Rev. B: Condens. Matter Mater. Phys.*, 2006, **74**, 035101.

50 B. R. Tuttle, S. M. Alhassan and S. T. Pantelides, *Phys. Rev. B: Condens. Matter Mater. Phys.*, 2015, **92**, 235405.

51 L. Keldysh, *JETP Lett.*, 1979, **29**, 658–661.

52 S. Andreev and T. Pavlova, *Phys. E*, 2008, **40**, 1551–1553.

53 M. D. Smith, L. Pedesseau, M. Kepenekian, I. C. Smith, C. Katan, J. Even and H. I. Karunadasa, *Chem. Sci.*, 2017, **8**, 1960–1968.

54 L. Pedesseau, D. Sapori, B. Traore, R. Robles, H.-H. Fang, M. A. Loi, H. Tsai, W. Nie, J.-C. Blancon, A. Neukirch, S. Tretiak, A. D. Mohite, C. Katan, J. Even and M. Kepenekian, *ACS Nano*, 2016, **10**, 9776–9786.

55 S. Chen and G. Shi, *Adv. Mater.*, 2017, **29**, 1605448.

56 S. Ahmad, P. K. Kanaujia, H. J. Beeson, A. Abate, F. Deschler, D. Credgington, U. Steiner, G. V. Prakash and J. J. Baumberg, *ACS Appl. Mater. Interfaces*, 2015, **7**, 25227–25236.

57 S. Saha, T. P. Sinha and A. Mookerjee, *Phys. Rev. B: Condens. Matter Mater. Phys.*, 2000, **62**, 8828–8834.